Effects of crystallinity on residual stresses via molecular dynamics simulations

Michail Papanikolaou, Francisco Rodriguez-Hernandez, Mark Jolly, and Konstantinos Salonitis
Manufacturing Theme, Cranfield University, Cranfield MK43 0AL, United Kingdom

(Received 8 May 2022; accepted 21 September 2022; published 5 October 2022)

Mechanical properties of materials are highly dependent on microstructure. One characteristic example is tensile stresses at the grain boundaries, which is one of the most critical factors in crack nucleation. Although experimental techniques have significantly evolved during the past decades with respect to obtaining high-resolution snapshots of the microstructure with methods such as scanning electron microscopy, the quantitative estimation of continuum quantities, such as localized stresses, still remains a very challenging task. The molecular dynamics simulation method has been proven to be a quite effective simulation tool for providing insights in such challenges due to its high spatial and temporal resolution. In this study, molecular dynamics simulations have been performed to obtain a spatial resolution of the residual stresses in solidified aluminum. A best-effort realistic microstructure was obtained by starting from a pure aluminum block which was initially melted and subsequently quenched under various cooling rates, and finally relaxed. The obtained results suggest that residual stresses are higher in absolute terms at the vicinity of grain boundaries than at the grain interiors, and higher crystallinity has been found to be correlated to lower residual stresses. Moreover, it has been shown both qualitatively and quantitatively that grain boundaries undergo tensile loading, in contrast to the grain interiors which are compressed; this result comes to support the conclusions of quite recent experimental investigations, showing that the residual stress is tensile at the grain boundaries and gradually transits into compressive in the grain interiors, and highlights the potential of molecular dynamics simulation to capture nanoscale physical phenomena.

DOI: 10.1103/PhysRevE.106.045302

I. INTRODUCTION

Residual stresses are defined as a type of stationary stress which remains in a solid body or material even after its cause has been removed [1]. They can be the result of any mechanical [2] or thermochemical [3,4] process and influenced by material properties including the heat capacity, plasticity, thermal conductivity, Young's modulus, and Poisson's ratio [5]. According to the pioneering study of Macherauch [6], residual stresses can be categorized according to different scales such as macroscopic and microscopic stress. Macroresidual stresses can be classified as type I, while microresidual stress as types II and III. Type I residual stresses are approximately homogeneous over large areas, much larger than the grain size, and are uniform over the material domain. Type II are homogeneous within a one-grain size or parts of grains and balance over a minimal number of grains, while type III residual stresses are not homogeneous at the atomic level and are uniformly distributed over small areas of a single grain.

Studies on residual stresses have been conducted since the early 1840s when the first quantitative analysis was established by Neumann's investigation [7]. Over the course of time, several qualitative and quantitative techniques have been developed to investigate residual stresses [8]. These methods compute strains and equivalent displacements instead of stresses, which can be implicitly evaluated based on several material parameters such as the modulus of elasticity or Poisson's ratio [9]. Residual stresses can be favorable or detrimental to the mechanical properties of the material. In a study on the benefits of residual stress conducted by Kandil *et al.* [10], the authors advocated that compressive residual stresses at the surface of brittle or ceramic materials increase the fatigue strength, cracking corrosion resistance, and bending strength. On the contrary, residual stresses can be very harmful to materials and downgrade their performance and the life cycle of the component [11]. The effect of residual tensile stress on material properties has been one of the most widely investigated topics. A study by Shiozaki *et al.* [12] reported that after a cyclic load during the punching process to manufacture holes in sheet steel, the fatigue strength was reduced at the hole edge due to the residual tensile stress induced during this process.

Due to the significant effects on mechanical properties of materials, researchers have attempted to measure residual stresses using experimental techniques. Zhang *et al.* [13] investigated the effects of the cooling rate on residual stresses via means of x-ray diffraction and finite-element analysis simulations. They controlled the cooling rate by immersing 2A14 alloy samples in water with varying initial temperature, ranging between 20 and 100 °C. They observed that residual stresses decline for lower cooling rates. Similar conclusions were drawn by Yi *et al.* [14], who measured the residual stresses using x-ray diffraction in Fe-B alloy specimens which were prepared under various cooling rates ranging between 0.1 and 30 K/s. The authors found that residual stresses were highly dependent on the cooling rate; more specifically, it was

 ©2022 American Physical Society

Published by the American Physical Society under the terms of the Creative Commons Attribution 4.0 International license.
Further distribution of this work must maintain attribution to the author(s) and the published article's title, journal "citation, and DOI.

shown that higher cooling rates lead to increasingly compressive residual stresses. The major limitation of experimental techniques for measuring residual stresses is low spatial resolution, while fracture and crack nucleation are phenomena mostly correlated with localized stress values. It has also been shown that the grain size, which is highly affected by the cooling rate, can introduce significant uncertainties in measuring residual stresses using diffraction techniques [15]. Experimental techniques have primarily been based on measuring residual stresses using averages; thus, they fail to capture residual stresses of type II and most importantly III. Only recently, Basu *et al.* [16] managed to obtain a spatial resolution of residual stresses via a hybrid electron backscattered diffraction and focused ion-beam digital image correlation method.

The molecular dynamics (MD) simulations method is a numerical simulation technique used to study the behavior of materials at the nanoscale level using cutting-edge computational facilities. Their high resolution renders MD capable of capturing stresses of both types II and III [6]. Numerous investigations have used MD simulations in several applications including solidification [17–20], solid deformation of materials [21,22], machining [23], and chemical processes [24]. Molecular dynamics has also been employed to model residual stresses. Guo *et al.* [25] were the first to perform molecular dynamics simulations to model residual stresses in nano- and polycrystalline copper. They developed polycrystalline copper microstructures, containing randomly oriented grains, and obtained a spatial resolution of residual stresses in the simulation domain. They expressed residual stresses using equivalent von Mises and hydrostatic stresses and showed that residual stresses are much higher at the grain-boundary regions. They also investigated the effects of the average grain size on residual stresses and showed that both von Mises and hydrostatic stresses drop for higher grain sizes. Finally, they presented the distribution of von Mises and stresses for various microstructures. Although their study was the first one to show the potential of molecular dynamics simulations to spatially resolve residual stresses, the grain-size distribution was not associated with the cooling rate but it was controlled via Voronoi tessellation parameters and no quantitative results on the average residual stresses distribution across different atom types were presented. Papanikolaou *et al.* [19] reproduced a spatial map of residual stresses in nanocrystalline aluminum using MD. Nanocrystalline structures were generated via melting an aluminum fcc block which was subsequently quenched and relaxed under various cooling rates. They reached conclusions similar to the ones presented in Guo *et al.* [25] and also obtained a qualitative measure of the evolution of residual stresses over time for all atoms. However, they did not examine the distribution of tensile stresses in their simulation domain and used only the von Mises stresses as a measure for residual stresses. Similarly to Ref. [25], they did not present any quantitative results on the interrelationship between atom types and residual stresses.

The present investigation aims at providing a spatial resolution of residual stresses in rapidly solidified metals and illustrating the interdependence of crystallinity and residual stresses. To obtain a best-effort realistic nanocrystalline aluminum, an aluminum block has been melted and subsequently quenched under various cooling rates and equilibrated according to the methodology presented in Ref. [18]. Various cooling rates were used to tune the grain-size distribution in the equilibrated structure; an alternative approach to control the grain size would be to vary the simulation pressure which affects the nucleation rate [26]. In addition to the previous MD studies on residual stresses, the present investigation offers a qualitative measure of residual stresses over the two main microstructure types encountered in solidified metals, i.e., crystals (grains) and amorphous (grain boundaries). Finally, the present study investigates the evolution of residual stresses using the hydrostatic stress, being indicative of the values of tensile residual stresses. It has been found that residual stresses tend to be tensile at the grain-boundary regions and compressive within the grain bodies. This result comes to support recent experimental investigations reaching the exact same conclusion and highlights the potential of MD simulations to capture nanoscale phenomena.

II. METHODOLOGY

The molecular dynamics workflow of this investigation consists of three main stages, namely (i) melting, (ii) quenching–solidification, and (iii) relaxation. The starting point was an aluminum (Al) block with dimensions of $25 \times 25 \times 25$ nm^3 containing 1×10^6 atoms positioned at the sites of a face-centered-cubic (fcc) lattice with a lattice constant of 4.05 Å [18]. The Al block was first relaxed at 273 K and subsequently isothermally heated up to 1173 K, which exceeds the melting point of aluminum by 240 K [27]. At 1173 K, 100% of the initial fcc structure was transformed into melt as shown in Fig. 1. According to Ref. [28], the aluminum atoms pass through the body-centered cubic (bcc) metastable phase during phase change.

Following equilibration, the melt was isothermally cooled down to 273 K. For the purposes of this study, four different cooling rates ranging between 0.5 and 4 K/ps have been used; these values led to a wide and representative variety of microstructures with very few (0.5 K/ps) to numerous (4 K/ps) grains, as it will be shown in the following sections. Following quenching, the block was relaxed for 100 000 time steps at 273 K until pressure and temperature were stabilized. Periodic boundary conditions were applied to all directions (x, y, and z). Moreover, the NPT (isothermal-isobaric) ensemble was used for both melting and solidification, while pressure and temperature were tuned via a barostat and a Nosé-Hoover thermostat. The corresponding temperature and pressure-damping coefficients were 1000 (2 ps) and 100 (0.2 ps) time steps respectively, according to the values proposed by previous MD studies [18].

To ensure accuracy, it was necessary to choose the most suitable interaction potential. Previous MD simulations [18,29,30] employed the Finnis-Sinclair (FS) potential [31] to model the interatomic interactions of aluminum. This is because Finnis-Sinclair potentials have an advantage over other interatomic potentials, such as Lennard-Jones (LJ) [32]; i.e., the atomic forces depend on the local atomic density. Moreover, FS potentials have been found to accurately reproduce key magnitudes related to the scope of this study including elastic constants, melting point, and vacancy formation energy

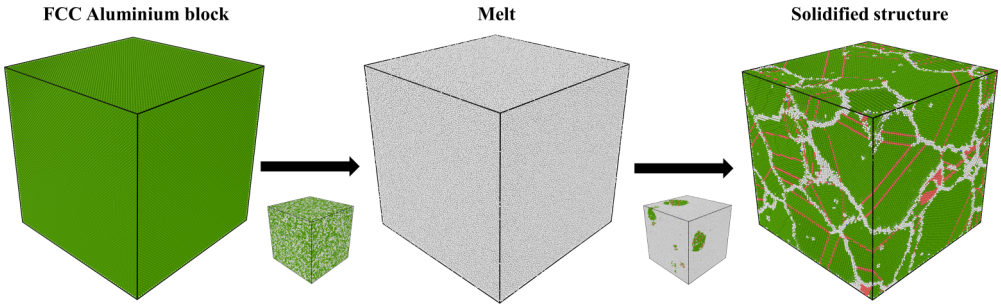


FIG. 1. Melting and equilibration process.

[33]. As it will be shown later, the estimated residual stresses are very close to the values proposed by other investigations. The Finnis-Sinclair potential is described by

$$E_{\text{tot}} = \sum_{i=1}^{N}\sum_{j=1}^{N} V_{ij}(r_{ij}) - A\sum_{i=1}^{N}\sqrt{\rho_i}. \tag{1}$$

In the expression above, E_{tot} is defined as the total energy, V_{ij} is the potential energy as a function of the interatomic distance r_{ij}, A is a potential parameter, and ρ_i is the local electron density given by

$$\rho_i = \sum_{j=1,\, i\neq j}^{N} \varphi_{ij}(r_{ij}), \tag{2}$$

where φ_{ij} is the local electron density. The potential energy of the *i-j* pair of atoms, V_{ij}, can be computed as follows:

$$V_{ij}(r_{ij}) = \begin{cases} (r_{ij}-c)^2\left(c_0 + c_1 r_{ij} + c_2 r_{ij}^2\right) & \text{if } r_{ij} \leqslant c \\ 0 & \text{if } r_{ij} > c. \end{cases} \tag{3}$$

In Eq. (3), c is the cutoff distance while the constants c_i are used to fit the potential energy to experimental results. The simulation parameters are listed in Table I.

The present investigation is focused on residual stress distribution of various structural atom types. To study the residual stress evolution and distribution during solidification and equilibration, four cooling rates ranging between 0.5 and 4 K/ps were considered. The Large-scale Atomic/Molecular Massively Parallel Simulator (LAMMPS) [34] was utilized for the MD simulations, and the OVITO PRO visualization tool [35] in conjunction with some complementary PYTHON was utilized to visualize, postprocess data, and extract meaningful continuum properties from atomistic simulations.

TABLE I. Simulation parameters.

Time step (fs)	2
Ensemble	*NPT*
Total number of atoms	1 000 000
Interatomic potential	Finnis-Sinclair
Cutoff distance (Å)	6
Simulation box dimensions (nm)	25 × 25 × 25
Boundary conditions	Periodic
Pressure (GPa)	0
Cooling rates (K/ps)	0.5, 1, 2, 4
Equilibration time (ps)	200

III. RESULTS AND DISCUSSION

In this section the effects of the quenching rate on nucleation, microstructure, and residual stress distribution will be discussed. Both qualitative and quantitative results have been obtained and discussed in the following subsections. Section III has been organized in four main subsections, namely Sec. III A, structural properties; Sec. 3 B, atom-type evolution; Sec. III C, nucleation; and Sec. III D residual stresses. The results presented in Secs. III B and III C have also been discussed in greater detail in Refs. [18,19].

A. Structural properties

The common neighbor analysis of Fig. 2 illustrates the evolution of the atomistic structure during the solidification process at various time steps for a cooling rate of 0.5 K/ps. The formation of fcc nuclei (green atoms) over time can be observed from the initial melt [white (amorphous) atoms]. The growth of fcc grains continues until the simulation domain temperature has reached about 507 K. By that point in time, fcc grains occupy most of the space, and grain boundaries, characterized by their amorphous structure, can be distinguished.

B. Atom-type evolution

To analyze the atom-type evolution during solidification, all atom-type populations were monitored over time for the examined cooling rates as shown in Fig. 3. The current analysis is focused on fcc, hexagonal-close packed (hcp), and amorphous atoms as bcc and icosahedral populations are almost negligible during solidification. The results show similar trends to previous studies [18,36]. Overall, the graphs illustrate a similar trend between them, i.e., the formation of fcc clusters is accompanied by a simultaneous and lower in volume increase of the HCP atoms and a significant reduction of the amorphous atoms.

Initially, the population of amorphous, fcc, and hcp atoms remains constant in the simulation domain (Fig. 3). The number of amorphous atoms starts decreasing dramatically while the fcc and hcp structures begin to form and grow concurrently. This trend is predominant until all atom-type populations reach an equilibrium stage. However, hcp atoms reach an asymptotic value, ranging between 50 000 and 100 000, sooner than the fcc and the amorphous ones; this indicates the premature formation of the hcp phase.

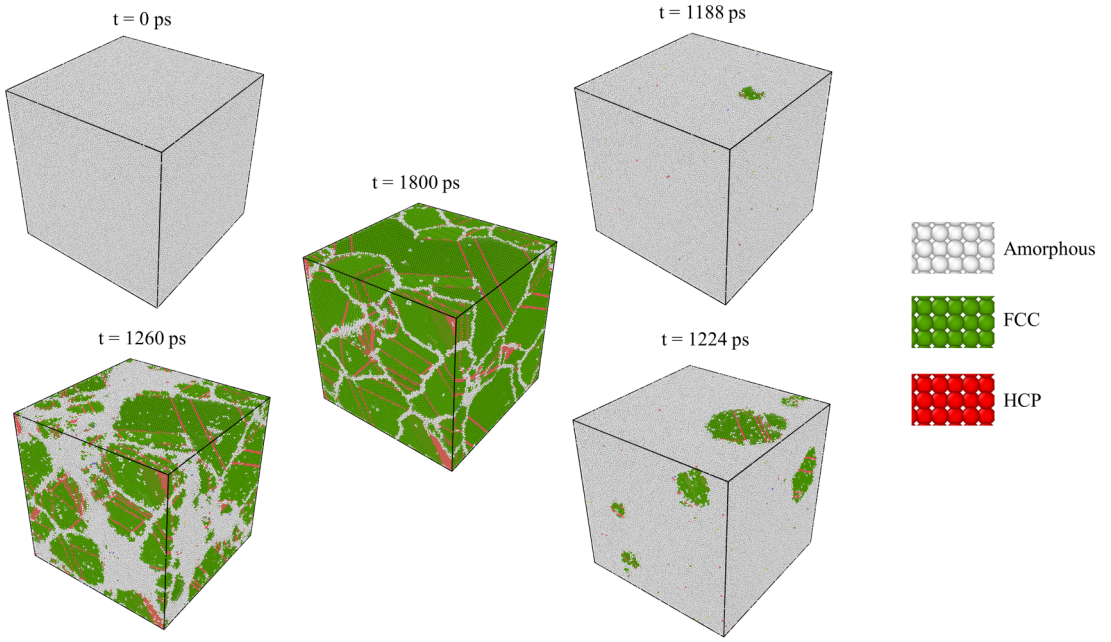


FIG. 2. Common neighbor analysis at various time steps ($c_R = 0.5$ K/ps).

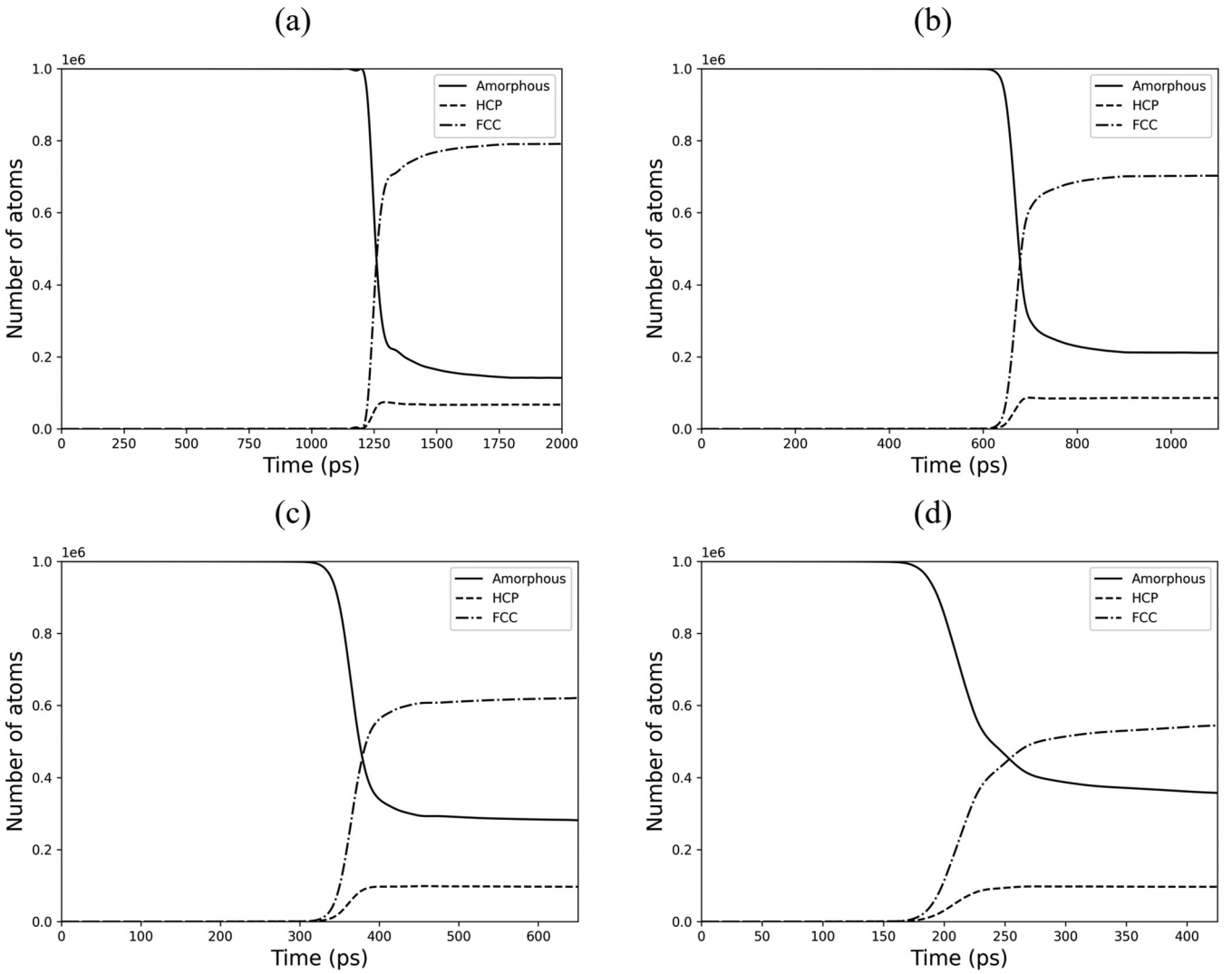


FIG. 3. Atom-type evolution for a cooling rate of (a) 0.5, (b) 1, (c) 2 K, and (d) 4 K/ps.

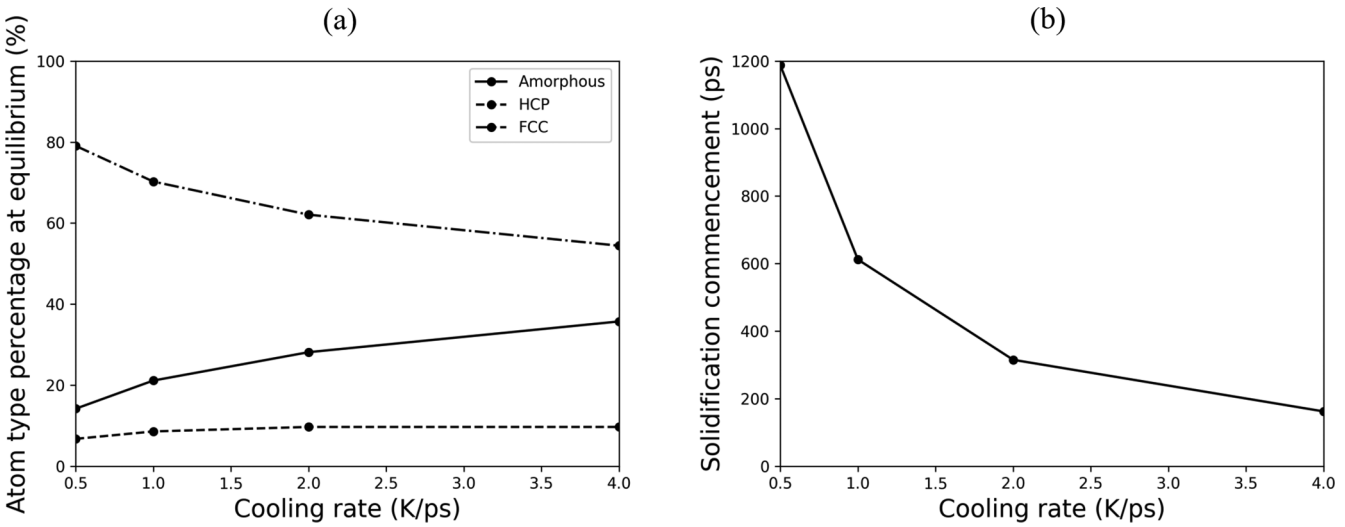


FIG. 4. (a) Atom types at equilibrium and (b) solidification commencement as a function of the cooling rate.

Figure 3 shows that higher cooling rates result in a reduced number of fcc atoms and increased amorphous and hcp populations at the equilibrated structure. This behavior is clearly illustrated in Fig. 4(a) and is attributed to the fact that supercooling favors the formation of amorphous structures instead of crystalline ones. Finally, the solidification commencement times have been plotted in Fig. 4(b); it can be observed that the higher the cooling rate the sooner the outset of solidification. More specifically, the solidification commencement time appears to be parabolically decreasing with cooling rate.

C. Nucleation

A 3D visualization of the solidified grain structure for each cooling rate following equilibration is shown in Fig. 5. For the calculation of the grain sizes, all grains were assumed to be spherical; thereby, the grain-size diameter d_g was estimated as follows:

$$\frac{4}{3}\pi\left(\frac{d_g}{2}\right)^3 = N\,V_a \Rightarrow d_g = 2\sqrt[3]{\frac{3NV_a}{4\pi}}, \tag{4}$$

where N is the total number of atoms of an fcc grain and V_a is the aluminum atom volume as calculated by the Voronoi analysis module of OVITO PRO [37].

The number of clusters at the end of the equilibration stage is dependent on the cooling rate. More specifically, faster cooling leads to a higher number of grains and smaller grains in the equilibrated structure. For faster cooling, nucleation can be triggered in many sites of the melt and consequently higher number of grains should be expected.

In order to analyze the effect of the cooling rate on the grain-size distribution, the average grain diameter $d_{g,\mathrm{ave}}$ was drawn as a function of the cooling rate in Fig. 6 ($d_{g,\mathrm{ave}}$ values correspond to the last time step of the equilibration stage). The mean grain size as a function of the cooling rate is characterized by a parabolic downward trend. As expected, for the

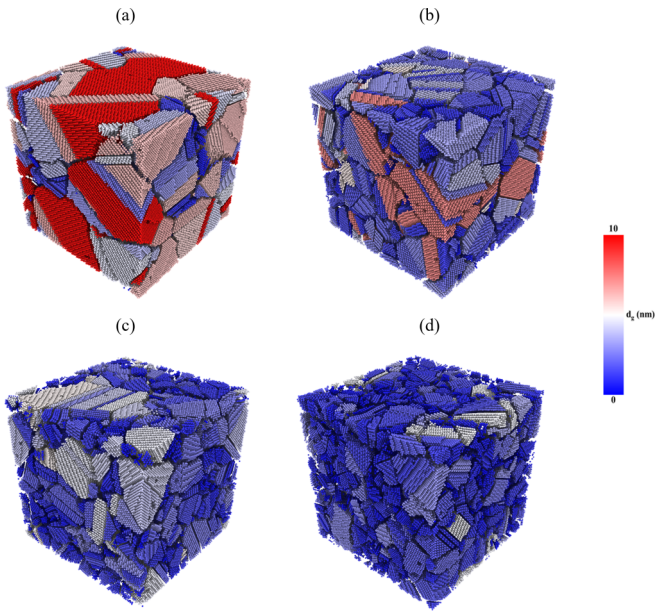


FIG. 5. Microstructure following equilibration for a cooling rate of (a) 0.5, (b) 1, (c) 2, and (d) 4 K/ps.

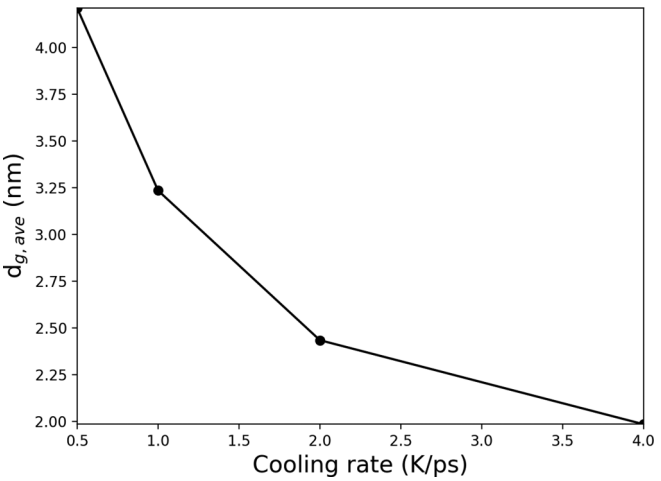


FIG. 6. Average grain diameter ($d_{g,\mathrm{ave}}$) following equilibration vs cooling rate.

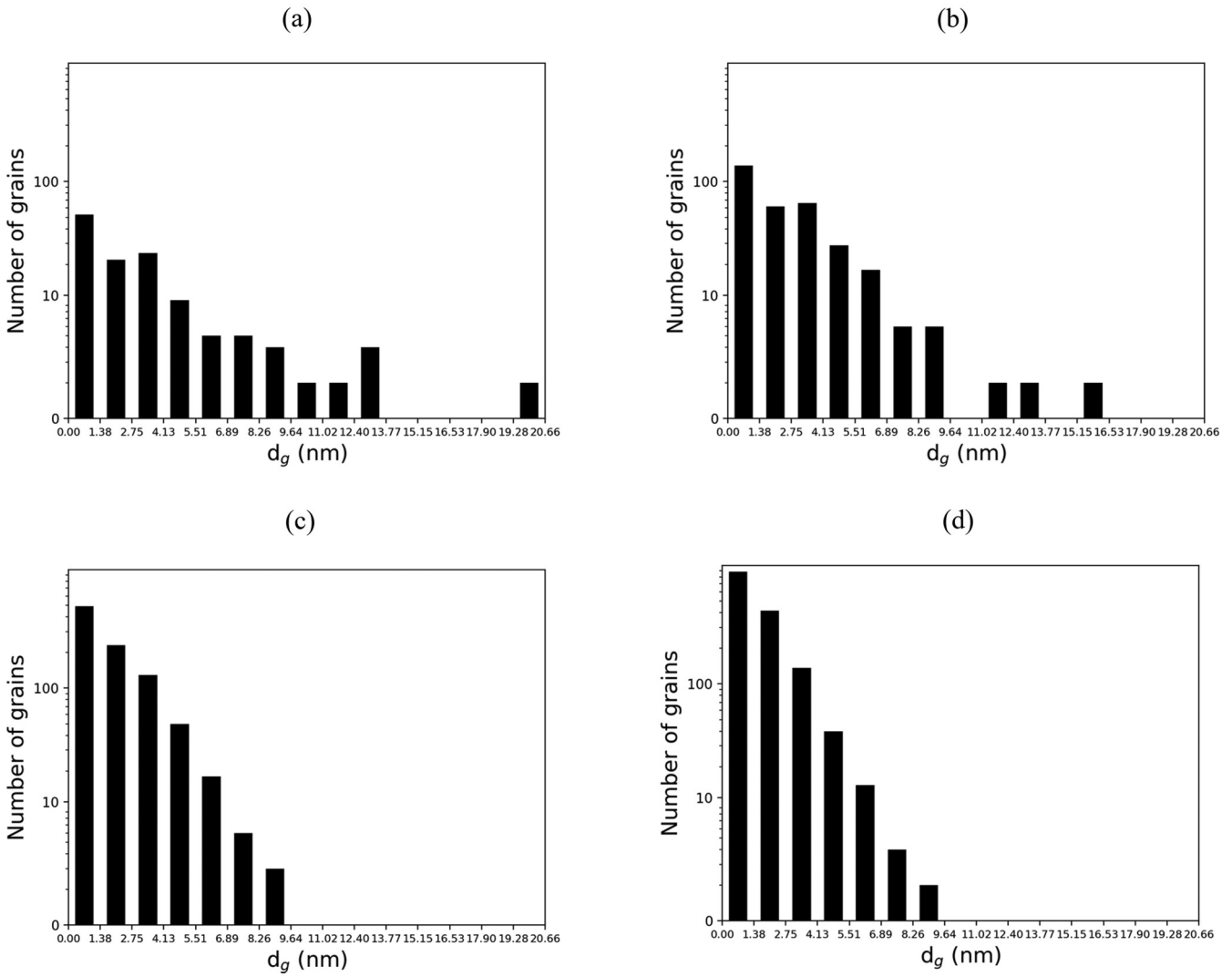


FIG. 7. Grain-diameter distribution for a cooling rate of (a) 0.5, (b) 1, (c) 2, and (d) 4 K/ps.

slowest cooling rate selected ($c_R = 0.5$ K/ps), the $d_{g,\text{ave}}$ value is just above 4 nm and this drops to 2 nm for $c_R = 4$ K/ps. This is again attributed to the dependence of microstructure on the cooling rate; for faster quenching the number of very small grains increases dramatically, and this results in the decrease of the measured average diameter.

In addition, the grain-size distribution for several cooling rates is plotted in Fig. 7. To effectively visualize the distribution of grain sizes for each cooling rate, grains were sorted in different size groups according to their diameter and their population was subsequently estimated. Overall, the bar charts of Fig. 7 show that the grain-diameter distribution is much wider for low cooling rates. It can be seen that the largest grain observed corresponds to the lowest cooling rate and has a diameter between 19.28 and 20.66 nm while the largest observed grain diameter for the fastest cooling rate is between 8.26 and 9.64 nm. Moreover, as pointed out above, the number of small grains increases dramatically for faster cooling. More specifically, the number of grains with a diameter between 0 and 1.38 nm, corresponding to a cooling rate of 0.5 K/ps, was just above 50, while this number climbed to 900 for the highest cooling rate examined (4 K/ps). The obtained grain sizes fall in the range of nanocrystalline aluminum ($d_{g,\text{ave}} <$ 100 nm) [38] and are similar to the grain sizes reproduced by similar MD studies [39]. However, it has to be mentioned that these values are far from experimental values of pure aluminum, which are in the range of hundreds of μm [40]. The reason for this is the very high cooling rates and spatial constraints that must be imposed in MD simulations given the current computational power limitations.

D. Residual stresses

In this subsection, the distribution of residual stresses within the simulation domain will be discussed. The equivalent von Mises stress (EVMS), which was used to represent residual stresses, is given by:

$$\sigma_{\text{VM}} = \sqrt{\frac{(\sigma_{xx} - \sigma_{yy})^2 + (\sigma_{yy} - \sigma_{zz})^2 + (\sigma_{zz} - \sigma_{xx})^2 + 6\left(\sigma_{xy}^2 + \sigma_{yz}^2 + \sigma_{zx}^2\right)}{2}}. \tag{5}$$

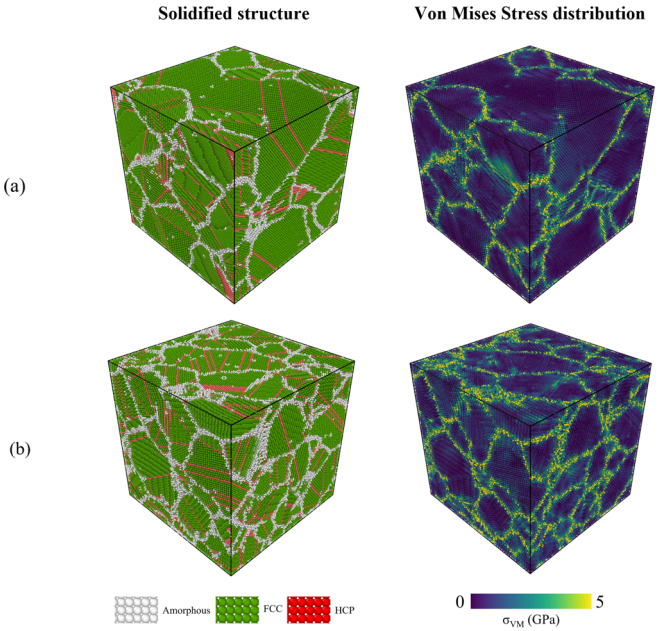


FIG. 8. CNA and von Mises (VM) stresses following quenching and relaxation for a cooling rate of (a) 0.5 and (b) 2 K/ps.

Figure 8 illustrates the CNA and EVMS distribution results at the end of quenching process for two cooling rates. The obtained von Mises (VM) values are very close to the spatial distribution of residual stresses snapshot obtained by Guo *et al.* [25]. From the comparative analysis between CNA and EVMS OVITO renders, it is evident that the grain boundaries present the highest residual stresses; this is in accordance with experimental studies [41]. On the other hand, in areas where the fcc phase is prevalent (grains), the residual stresses are about equal to zero. Moreover, Fig. 8 shows a high residual stress concentration near hcp lattice structure which denotes lattice dislocations. According to Ref. [42], dislocation initiation and propagation are associated with high stress concentration and therefore, residual stresses could be the underlying reason for this behavior.

In addition, a wider quantitative analysis to study the evolution of the residual stresses over the simulation domain has been conducted. The average residual stress per atom ($\sigma_{\mathrm{VM,ave}}$) has been estimated as follows:

$$\sigma_{\mathrm{VM,\ ave}} = \frac{1}{N}\sum_{i=1}^{N}\sigma_{\mathrm{VM},\ i}, \tag{6}$$

and plotted in Fig. 9 over time for the selected cooling rates. In general, it is shown that all cooling rates exhibit a similar trend of the $\sigma_{\mathrm{VM,ave}}$ value over solidification and equilibration. Moreover, it is evident that the initial $\sigma_{\mathrm{VM,ave}}$ value is constant and proportional to the cooling rate. These results are in agreement with previous investigations [19] where the analogy that thermal stresses are proportional to cooling rates was used to explain these phenomena. In the following stage, $\sigma_{\mathrm{VM,ave}}$ value begins to sharply increase before it enters a fluctuation interval before stabilizing. As expected, the extended grain boundary and lattice dislocation area, owing to faster cooling, led to a higher final value of the average residual stress.

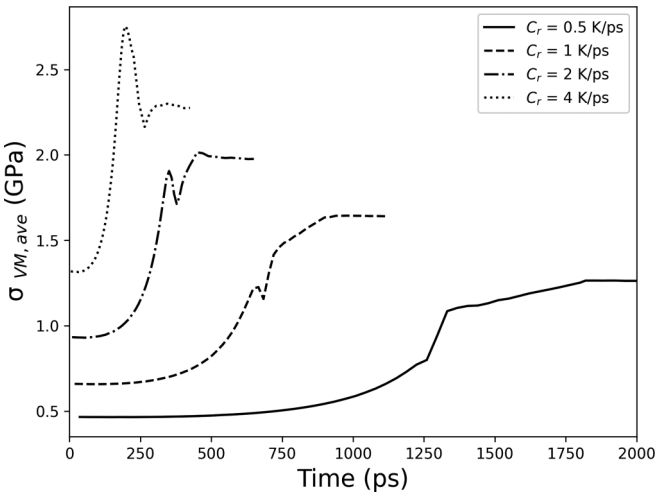


FIG. 9. Average σ_{VM} as a function of time.

To further investigate the fluctuations observed in Fig. 9, the number of grains has been plotted against time for various cooling rates in Fig. 10. In general, a similar trend is presented for each one of the cooling rates examined, i.e., the population of grains sharply increases and reaches a peak. Later on, it begins to decrease until it asymptotically reaches a constant value. The underlying reason for this behavior will be analyzed in the following paragraph. By comparing Fig. 9 and Fig. 10, it can be observed that residual stresses and grain population increase dramatically following the same trend at the same time.

It is well known that crystallization is an exothermic process during which latent heat is released [18]. In the vicinity of regions with elevated temperature due to the latent heat release, some grains might concatenate with their neighbors, a behavior also known as "coarsening" [36]. As a result, residual stresses are relieved during coarsening, and this explains the downward step observed in all curves of Fig. 9. The behavior discussed above is more dominant for fast quenching because the latent heat is concurrently released at various regions of the simulation domain because faster quenching leads

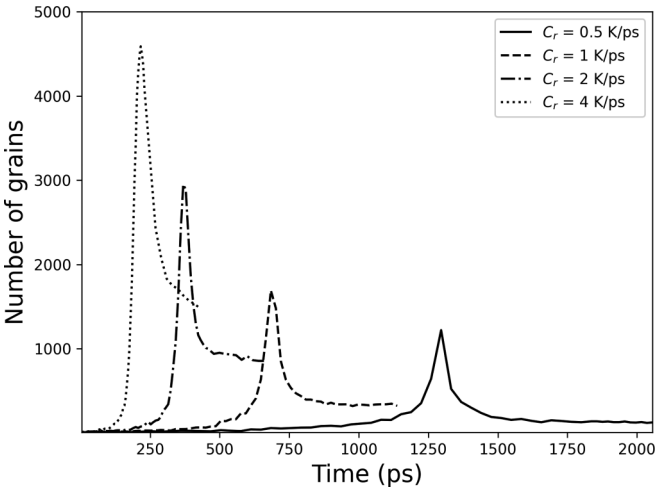


FIG. 10. Number of grains vs time.

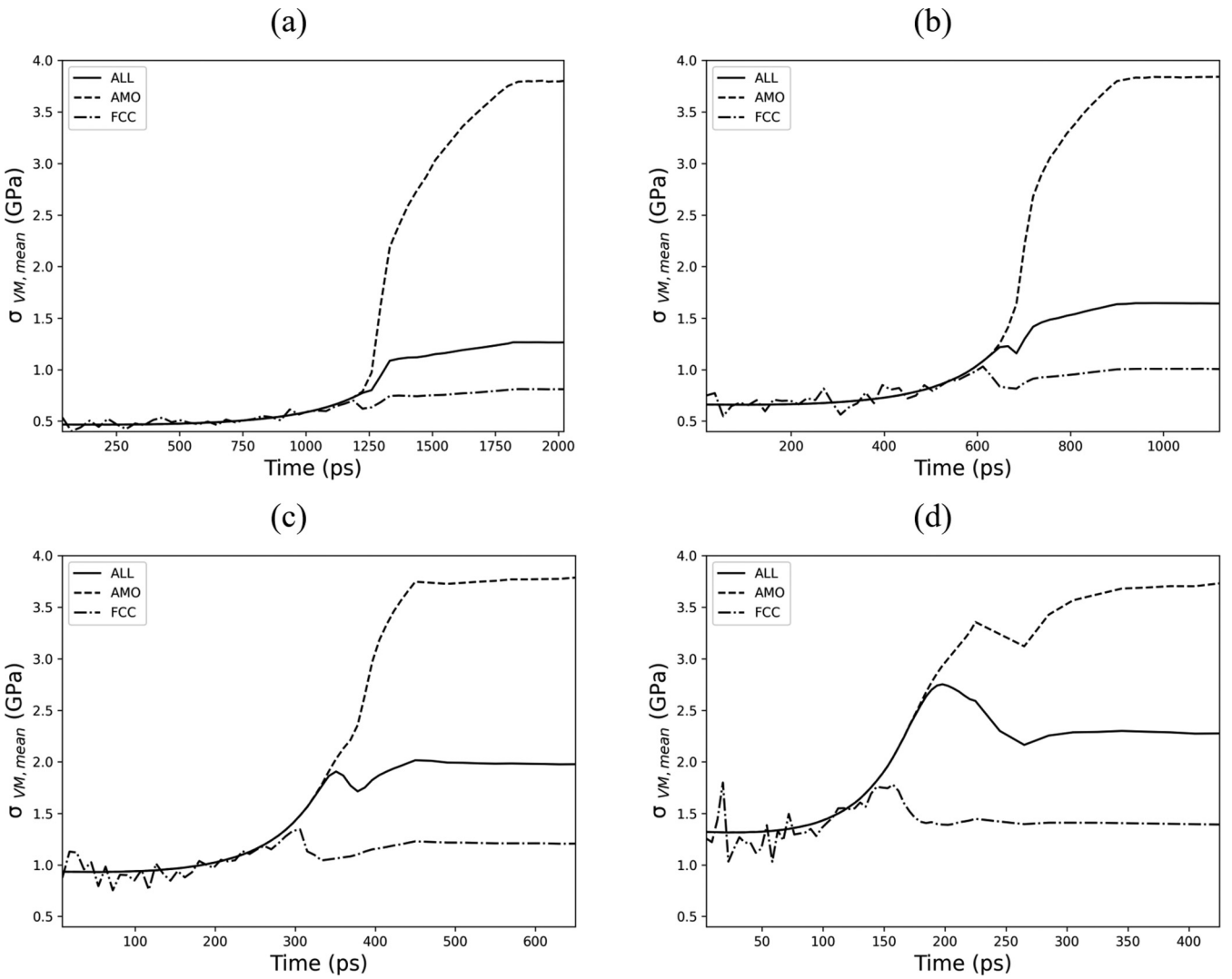


FIG. 11. Average σ_{VM} vs time for a cooling rate of (a) 0.5, (b) 1, (c) 2, and (d) 4 K/ps.

to a higher number of grains as discussed above. For the same reason, this downward step of the residual stresses cannot be clearly distinguished for a cooling rate of 0.5 K/ps (Fig. 9). After this step, residual stresses maintain an increasing trend for a short time interval before stabilizing; this is because interatomic bonds become stronger and potential energy increases, in absolute terms, during cooling and equilibration.

Figure 11 illustrates the average VM stress of various atom types as a function of time for the examined cooling rates. Overall, all plots exhibit a similar trend: the amorphous atoms reach a higher average VM residual stress value compared to fcc atoms. The average VM residual stresses for all atom types, fcc, and amorphous presents similar trends to the ones of Fig. 9. It is evident that the residual stresses for all atom types start to increase as solidification progresses, as expected. Moreover, it can be observed that residual stresses start increasing at an earlier timepoint for faster cooling rates, as expected.

Following their initial increase, the residual stresses of fcc atoms undergo a fluctuation period before they reach equilibrium. This trend is similar for all cases analyzed in this investigation and is attributed to the coarsening phenomenon as discussed above. However, this behavior cannot be observed for the amorphous atoms (residual stresses do not fluctuate) except for the highest cooling rate examined [Fig. 11(d)], where the residual stresses of amorphous atoms decline in the time span between 225 and 275 ps. The reduction of the residual stresses of the amorphous atoms, for a cooling rate of 4 K/ps following their peak, is due to the concurrent latent-heat release at many sites (grains) of the simulation domain. This affects both the population and the average stress of amorphous atoms. More specifically, the concurrent latent-heat release leads to the relaxation of stresses at the grain boundaries which is reflected by the decreasing trend in the residual stresses of the amorphous atoms. Subsequently, residual stresses continue increasing as the absolute potential energy keeps climbing.

The total von Mises stress as a function of time for different atom types and cooling rates has been plotted in Fig. 12. In general, all simulated cooling rates show similar trends. It can be observed that the total VM residual stress ($\sigma_{\mathrm{VM,sum}}$) of amorphous atoms starts increasing slightly while the corresponding value for fcc atoms remains constant and equal to 0 for a cooling rate equal to 0.5 K/ps. As mentioned above,

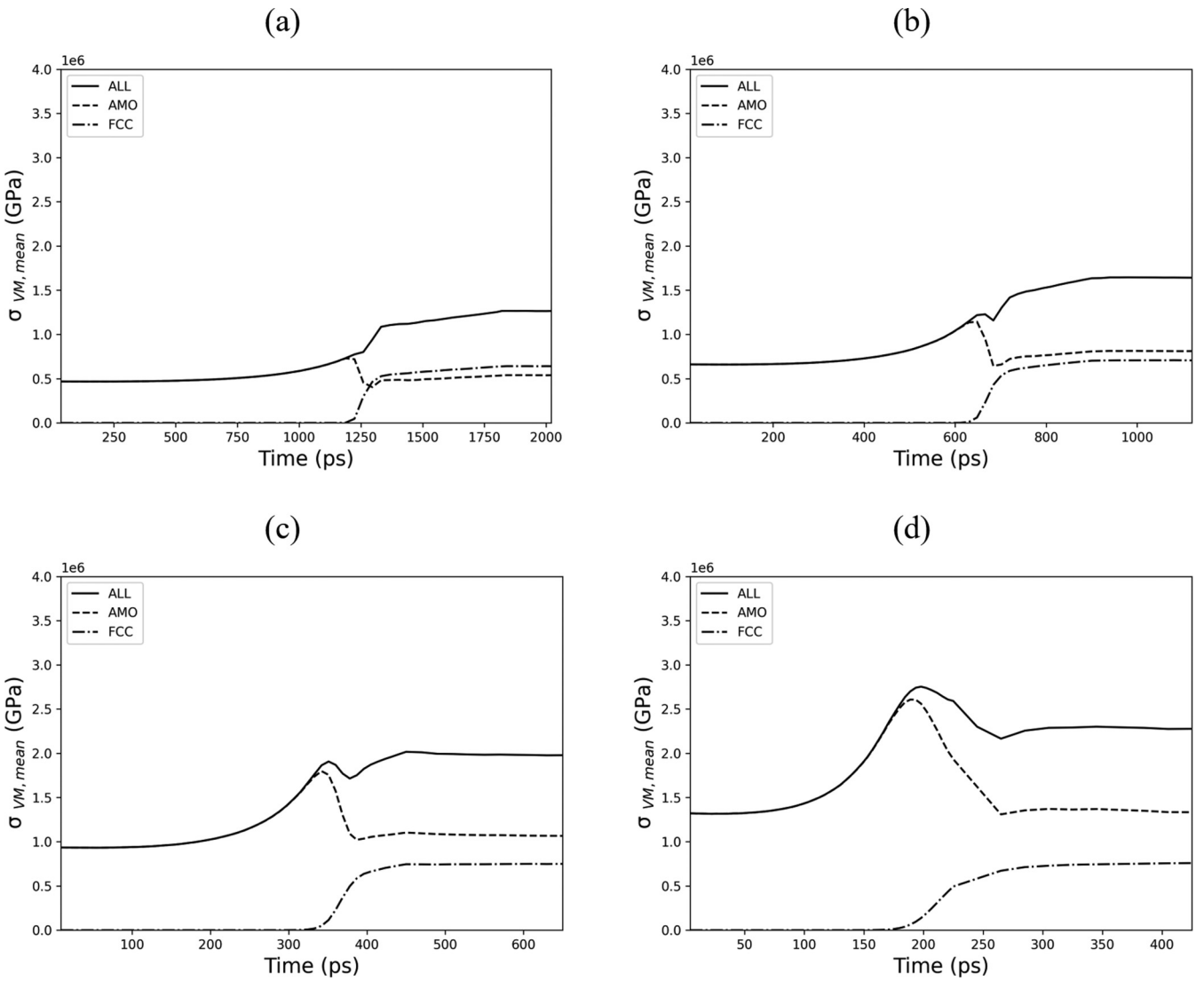


FIG. 12. Total σ_{VM} vs time for a cooling rate of (a) 0.5, (b) 1, (c) 2, and (d) 4 K/ps.

this initial slope and its starting point are dependent on the cooling rate since it is more pronounced for higher cooling rates. It can be discerned that the amorphous $\sigma_{\mathrm{VM,sum}}$ value starts decreasing sharply as the fcc $\sigma_{\mathrm{VM,sum}}$ value begins to rise at the same time. This trend is maintained until the residual stresses reach an equilibrium point. Moreover, for higher cooling rates, the difference between the amorphous and fcc VM residual stresses becomes higher. For $c_R = 0.5$ K/ps the residual stresses of fcc atoms are higher compared to the amorphous ones while for $c_R = 4$ K/ps this trend is reversed, and their difference exceeds 1 GPa. The reason for this is that higher cooling rates favor the increase of the area of the grain boundaries as well as the population of amorphous atoms; this in turn leads to higher concentration of residual stresses at the grain boundaries compared to the grains. Finally, it should be mentioned that higher cooling rates appear to predominantly affect the residual stresses at the grain boundaries and not at the cores of the grains. The final (equilibrated) total residual stresses value for fcc atoms climbed from ~ 0.6 to ~ 0.75 GPa (increase of 0.15 GPa) as the cooling rated increased from 0.5 to 4 K/ps, while the corresponding increment in the total residual stresses of amorphous atoms exceeded 0.8 GPa.

Residual stresses are useful for expressing the magnitude of residual stresses over the simulation domain. However, the

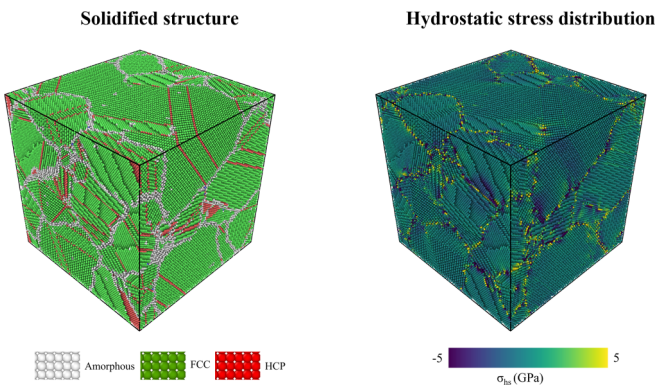


FIG. 13. CNA and hydrostatic stress following quenching and relaxation ($c_R = 0.5$ K/ps).

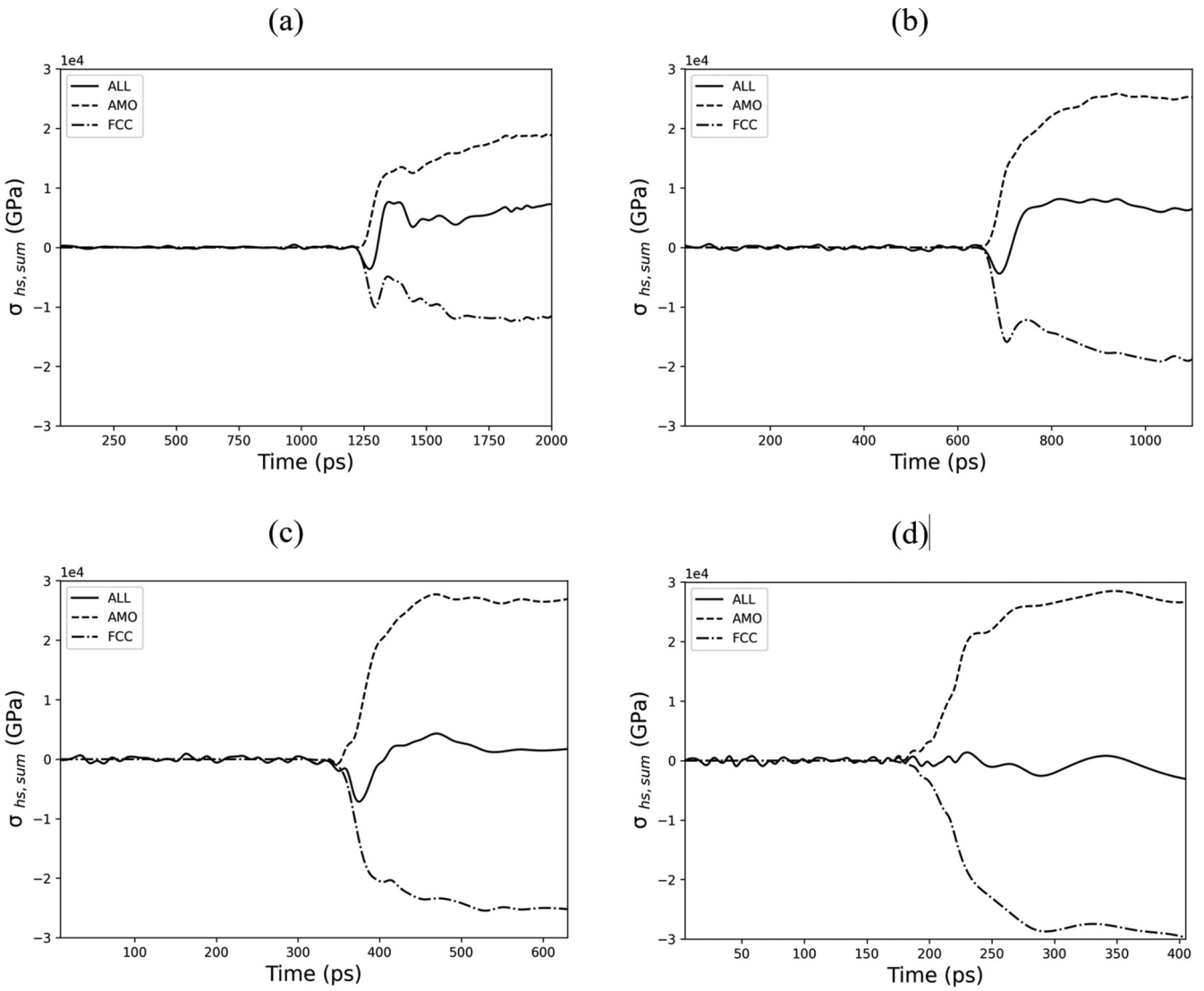


FIG. 14. Total $\sigma_{\rm hs}$ vs time for a cooling rate of (a) 0.5, (b) 1, (c) 2, and (d) 4 K/ps.

mechanical behavior of materials is dependent on the applied tensile stresses. In this study, the hydrostatic stress ($\sigma_{\rm hs}$), calculated according to (6), was used to examine tensile stress distribution over the simulation domain:

$$\sigma_{\rm hs} = \frac{\sigma_{xx} + \sigma_{yy} + \sigma_{zz}}{3}. \tag{7}$$

As illustrated in Fig. 13, tensile stresses vary between tensile and compressive across the simulation domain. From a first glance, it appears that grain-boundary atoms undergo tensile loading. On the contrary, stresses at the grain bodies appear to be zero or even compressive. In order to make safer conclusions about the nature of the hydrostatic stresses, their sums were plotted as per each atom type for all cooling rates in Fig. 14. By comparing Fig. 12 and Fig. 14**,** it can be seen that tensile stresses are much lower than von Mises. Most importantly though, it appears that the nature of the tensile stresses changes with the atom type and consequently the microstructure. More specifically, it can be observed that fcc atoms are compressed, in contrast to the grain-boundary atoms which undergo tensile loading. It is worthwhile to note that this observation is in agreement with the experimental results of Basu *et al.* [16], who used a focused ion-beam–digital image-correlation technique to measure spatial stress gradients at the vicinity of grain boundaries. More specifically, the authors of this study observed that the stress distribution in pure titanium is tensile at the grain boundaries and gradually transits into compressive in the grain interiors. Similar experimental observations have also been made for transparent conductive oxide films [43]. The underlying physical mechanism could be that as grains try to grow in a confined space during solidification and cooling, they start compressing each other. Their tendency to grow leads to the development of frictionlike forces at the grain boundaries which are translated to tensile loading at these areas.

IV. CONCLUSIONS

In this study, the influence of the cooling rate on residual stress evolution and distribution was investigated with the help of three-dimensional molecular dynamics simulations. The grain structure as well as key magnitudes such as the

potential energy and the grain-size evolution during solidification were used to interpret the behavior of residual stresses. The main findings of this investigation are briefly summarized below:

(i) Amorphous atoms, located at the grain boundaries, and hcp atoms at the vicinity of lattice dislocations accumulate high residual stresses compared to fcc atoms of the grains.

(ii) Faster quenching induces an increase in the grain-boundary area and lattice dislocations for high cooling rates and consequently, an increase of the total residual stresses.

(iii) It has been found that the residual stress distribution per atom type is influenced by the cooling rate. More specifically, high cooling rates favor the formation of amorphous atoms, and consequently, an increment of residual stress at the grain-boundary areas can be observed.

(iv) Tensile loads are applied to the grain-boundary atoms and compressive loads at the crystal grains. This result is in agreement with quite recent experimental investigations showing that residual stress is tensile at the grain boundaries and gradually transits into compressive in the grain interiors.

ACKNOWLEDGMENT

This research was funded by the UK EPSRC project "Energy Resilient Manufacturing 2: Small Is Beautiful Phase 2 (SIB2)" under Grant No. EP/P012272/1.

[1] P. J. Withers and H. K. D. H. Bhadeshia, Residual stress. Part 1 – Measurement techniques, Mater. Sci. Technol. **17**, 355 (2013).

[2] P. J. Withers and H. K. D. H. Bhadeshia, Residual stress. Part 2 - Nature and origins, Mater. Sci. Technol. **17**, 366 (2013).

[3] G. P. Dolan and J. S. Robinson, Residual stress reduction in 7175-T73, 6061-T6 and 2017A-T4 aluminium alloys using quench factor analysis, J. Mater. Process. Technol. **153–154**, 346 (2004).

[4] F. Fanicchia, X. Maeder, J. Ast, A. A. Taylor, Y. Guo, M. N. Polyakov, J. Michler, and D. A. Axinte, Residual stress and adhesion of thermal spray coatings: Microscopic view by solidification and crystallisation analysis in the epitaxial CoNiCrAlY single splat, Mater. Des. **153**, 36 (2018).

[5] T. Inoue and Z. Wang, Coupling between stress, temperature, and metallic structures during processes involving phase transformations, Mater. Sci. Technol. (United Kingdom) **1**, 845 (1985).

[6] E. Macherauch, Introduction To Residual Stress., in Adv. in Sur Treat, Technol. - Appl. - Eff., Vol. 4 (Pergamon Press, Oxford, 1987), pp. 1–36.

[7] K. E. Neumann, Die Gesetze Der Doppelbrechung Des Lichts in Comprimirten Oder Ungleichförmig Erwärmten Unkrystallinischen Körpern, Ann. Phys. **130**, 449 (1841).

[8] J. Lu, *Handbook of Measurement of Residual Stresses* (Fairmont Press, Lilburn GA; Upper Saddle River NJ, 1996), Vol. 34.

[9] J. GUO, H. FU, B. PAN, and R. KANG, Recent progress of residual stress measurement Methods: a review, Chinese J. Aeronaut. **34**, 54 (2021).

[10] F. A. Kandil, J. D. Lord, A. T. Fry, and P. V. Grant, *A Review of Residual Stress Measurement Methods-A Guide to Technique Selection* (National Physics Laboratory, Teddington, Middlesex, UK, 2001).

[11] M. Gurr and R. Mülhaupt, Rapid Prototyping, Ref. Modul. Mater. Sci. Mater. Eng. 1 (2016).

[12] T. Shiozaki, Y. Tamai, and T. Urabe, Effect of residual stresses on fatigue strength of high strength steel sheets with punched holes, Int. J. Fatigue **80**, 324 (2015).

[13] Y.-x. Zhang, Y.-p. Yi, S.-q. Huang, and F. Dong, Influence of quenching cooling rate on residual stress and tensile properties of 2A14 aluminum alloy forgings, Mater. Sci. Eng. A **674**, 658 (2016).

[14] Y. Yi, Q. Li, J. Xing, H. Fu, D. Yi, Y. Liu, and B. Zheng, Effects of cooling rate on microstructure, mechanical properties, and residual stress of Fe-2.1B (Wt%) alloy, Mater. Sci. Eng. A **754**, 129 (2019).

[15] R. C. Wimpory, R. V. Martins, M. Hofmann, J. R. Kornmeier, S. Moturu, and C. Ohms, A complete reassessment of standard residual stress uncertainty analyses using neutron diffraction emphasizing the influence of grain size, Int. J. Press. Vessel. Pip. **164**, 80 (2018).

[16] I. Basu, V. Ocelík, and J. T. M. De Hosson, Measurement of spatial stress gradients near grain boundaries, Scr. Mater. **136**, 11 (2017).

[17] K. Vijay Reddy, M. Meraj, and S. Pal, Presence of retained crystalline seed necessary for bicrystal-liquid-bicrystal phase transformation, J. Cryst. Growth **475**, 307 (2017).

[18] M. Papanikolaou, K. Salonitis, M. Jolly, and M. Frank, Large-scale molecular dynamics simulations of homogeneous nucleation of pure aluminium, Metals (Basel). **9**, 1217 (2019).

[19] M. Papanikolaou, K. Salonitis, and M. Jolly, Molecular dynamics simulations of the evolution of residual stresses during rapid solidification of aluminium, Miner., Met. Mater. Ser. **6**, 918 (2021).

[20] T. Shen, W. Meng, Y. Wu, and X. Lu, Size dependence and phase transition during melting of fcc-Fe nanoparticles: A molecular dynamics simulation, Appl. Surf. Sci. **277**, 7 (2013).

[21] K. V. Reddy and S. Pal, Dynamic probing of structural evolution of single crystal Fe during rolling process using atomistic simulation, Steel Res. Int. **90**, 1800636 (2019).

[22] K. V. Reddy, C. Deng, and S. Pal, Dynamic characterization of shock response in crystalline-metallic glass nanolaminates, Acta Mater. **164**, 347 (2019).

[23] Y. Li, M. Shuai, J. Zhang, H. Zheng, T. Sun, and Y. Yang, Molecular dynamics investigation of residual stress and surface roughness of cerium under diamond cutting, Micromachines **9**, 386 (2018).

[24] S. James and K. Shah, Effect of velocity and impact angle on residual stress generation in cold spray process-A molecular dynamics simulation study, Procedia Manuf. **48**, 776 (2020).

[25] Y.-B. Guo, T. Xu, and M. Li, Atomistic calculation of internal stress in nanoscale polycrystalline materials, Philos. Mag. **92**, 3064 (2012).

[26] Z. Han, X. Huang, A. A. Luo, A. K. Sachdev, and B. Liu, A quantitative model for describing crystal nucleation in pressurized solidification during squeeze casting, Scr. Mater. **66**, 215 (2012).

[27] R. P. Verma and M. Kumar Lila, A short review on aluminium alloys and welding in structural applications, Mater. Today Proc. **46**, 10687 (2021).

[28] Y. Shibuta, S. Sakane, E. Miyoshi, S. Okita, T. Takaki, and M. Ohno, Heterogeneity in homogeneous nucleation from billion-atom molecular dynamics simulation of solidification of pure metal, Nat. Commun. **8**, 10 (2017).

[29] Y. Shibuta, S. Sakane, T. Takaki, and M. Ohno, Submicrometer-scale molecular dynamics simulation of nucleation and solidification from undercooled melt: Linkage between empirical interpretation and atomistic nature, Acta Mater. **105**, 328 (2016).

[30] M. Papanikolaou, K. Salonitis, and M. Jolly, Molecular Dynamics Simulations of the Solidification of Pure Aluminium, in *Light Metals* (Springer, Cham, 2020), pp. 158–167.

[31] M. W. Finnis and J. E. Sinclair, A simple empirical n-body potential for transition metals, Philos. Mag. A **50**, 45 (1984).

[32] X. Wang, S. Ramírez-Hinestrosa, J. Dobnikar, and D. Frenkel, The Lennard-Jones potential: When (not) to use it, Phys. Chem. Chem. Phys. **22**, 10624 (2020).

[33] A. E. Galashev, L. A. Elshina, and R. V. Muradymov, Molecular dynamic study of the mechanism of formation of 2D carbon nanostructures in a solid Al–C nanocomposite grain, J. Phys. Chem. A **90**, 2444 (2016) (in Russian).

[34] *LAMMPS Molecular Dynamics Simulator*, https://lammps.sandia.gov/.

[35] A. Stukowski, *Ovito Open Visualization Tool*.

[36] Z. Y. Hou, K. J. Dong, Z. A. Tian, R. S. Liu, Z. Wang, and J. G. Wang, Cooling rate dependence of solidification for liquid aluminium: A large-scale molecular dynamics simulation study, Phys. Chem. Chem. Phys. **18**, 17461 (2016).

[37] A. Stukowski, Structure identification methods for atomistic simulations of crystalline materials, Model. Simul. Mater. Sci. Eng. **20**, 45021 (2012).

[38] W. Hanna, K. Maung, M. Enayati, J. C. Earthman, and F. A. Mohamed, Grain size stability in a cryomilled nanocrystalline Al alloy powders containing diamantane nanoparticles, Mater. Sci. Eng. A **746**, 290 (2019).

[39] A. Mahata, M. A. Zaeem, and M. I. Baskes, Understanding homogeneous nucleation in solidification of aluminum by molecular dynamics simulations, Model. Simul. Mater. Sci. Eng. **26**, 025007 (2018).

[40] Z. Chen and K. Yan, Grain refinement of commercially pure aluminum with addition of Ti and Zr elements based on crystallography orientation, Sci. Rep. **10**, 16591 (2020).

[41] V. R. Vedula, S. J. Glass, D. M. Saylor, G. S. Rohrer, W. C. Carter, S. A. Langer, and E. R. Fuller, Residual-stress predictions in polycrystalline alumina, J. Am. Ceram. Soc. **84**, 2947 (2001).

[42] M. Papanikolaou, F. R. Hernandez, and K. Salonitis, Investigation of the subsurface temperature effects on nanocutting processes via molecular dynamics simulations, Metals (Basel). **10**, 1220 (2020).

[43] K. H. Ri, Y. Wang, W. L. Zhou, J. X. Gao, X. J. Wang, and J. Yu, The structural properties of Al doped ZnO films depending on the thickness and their effect on the electrical properties, Appl. Surf. Sci. **258**, 1283 (2011).



https://dspace.org/

Effects of crystallinity on residual stresses via molecular dynamics simulations

Papanikolaou, Michail; Rodriguez-Hernandez, Francisco; Jolly, Mark R.; Salonitis, Konstantinos

2022-10-05
American Physical Society
https://doi.org/10.1103/PhysRevE.106.045302
Papanikolaou M, Rodriguez-Hernandez F, Jolly M, Salonitis K. (2022) Effects of crystallinity on residual stresses via molecular dynamics simulations. Physical Review E, Volume 106, October 2022, Article number 045302

Downloaded from a DSpace repository. https://dspace.org/